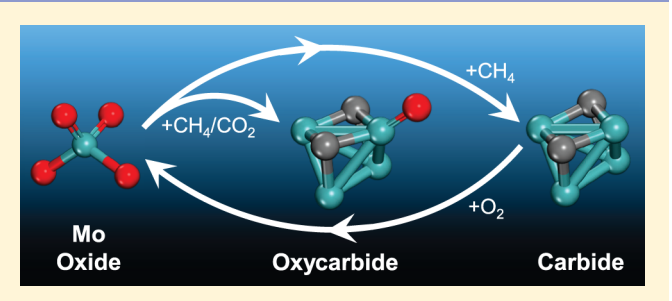


Molybdenum Oxide, Oxycarbide, and Carbide: Controlling the Dynamic Composition, Size, and Catalytic Activity of Zeolite-**Supported Nanostructures**

Yiteng Zheng, Yadan Tang, James R. Gallagher, Jie Gao, Jeffrey T. Miller, Jie Gao, Gallagher, Jie Gao, Jeffrey T. Miller, Simon G. Podkolzin, Jeffrey T. Miller, Jef

Supporting Information

ABSTRACT: Molybdenum nanostructures are promising catalysts for a single-step methane conversion into aromatic hydrocarbons and for multiple other hydrocarbon reactions. Dynamic transformations of catalytic zeolite-supported Mo structures from an oxide to an oxycarbide and then to a carbide in methane dehydroaromatization were studied with in situ Xray absorption spectroscopic measurements and density functional theory calculations. After a treatment in the presence of gas-phase oxygen, Mo is present in the form of isolated oxide structures. Under reaction conditions with methane, these



initial oxide structures become carbided and catalyze methane conversion to aromatic hydrocarbons. As the reaction progresses, the Mo carbide structures agglomerate and accumulate excess carbon, leading to catalyst deactivation. Although the initial oxide structures and catalytic activity can be restored by reversing the agglomeration and coking with periodic oxygen regeneration treatments, it is desirable to continuously control the dynamic composition, size and catalytic activity of Mo structures under hydrocarbon reaction conditions. This objective can be accomplished by co-feeding an oxygen-containing molecule, such as CO₂, that transforms Mo structures into an oxycarbide and slows the undesirable agglomeration and coking. It is, therefore, preferable for preserving catalytic activity to prevent full carburization of Mo and, instead, maintain the Mo structures in an oxycarbide form, an intermediate between an oxide and a carbide.

1. INTRODUCTION

Bulk and nanodisperse molybdenum oxide, oxycarbide and carbide structures are actively studied for multiple applications in diverse areas of science and technology: from catalysis 1-5 to superconducting materials,⁶ solar cells,⁷ and batteries.^{8,9} In catalysis, Mo structures were found to be effective in a broad range of reactions: natural gas conversion, water-gas shift reaction,^{2,3} hydrogen production,^{4,10} olefin epoxidation⁵ and biomass upgrading.11-14

Molybdenum nanostructures supported on a zeolite, such as ZSM-5, are promising catalysts for natural gas conversion into aromatic hydrocarbons in a single step. 1,15-18 The main reaction is methane dehydroaromatization with the formation of benzene and hydrogen: 6CH₄ = C₆H₆ + 9H₂. During catalyst preparation, a treatment with gas-phase O2 at an elevated temperature produces isolated Mo oxide structures. Under reaction conditions with methane, these initially highly dispersed Mo oxide nanostructures convert into carbided

structures and agglomerate into nanoparticles. One of the main reasons for rapid catalyst deactivation is a loss of accessible Mo sites due to agglomeration and formation of a carbon overlayer. $^{18-23}$ Our recent study demonstrates that the agglomeration and coking can be reversed and the initial catalytic activity can be restored by stopping the reaction with methane and performing an O2 treatment. Although regeneration with O2 is effective, it is preferable to identify methods for maintaining the catalytic activity by continuously controlling the composition and size of Mo nanostructures under hydrocarbon reaction conditions instead of completely stopping the reaction and performing periodic regeneration treatments.

Received: June 7, 2019 Revised: August 3, 2019 Published: August 9, 2019



[†]Department of Chemical Engineering and Materials Science, Stevens Institute of Technology, Hoboken, New Jersey 07030, United

[‡]Operando Molecular Spectroscopy & Catalysis Laboratory, Department of Chemical and Biomolecular Engineering, Lehigh University, Bethlehem, Pennsylvania 18015, United States

[§]Chemical Science and Engineering Division, Argonne National Laboratory, Argonne, Illinois 60439, United States

Davidson School of Chemical Engineering, Purdue University, West Lafayette, Indiana 47907, United States

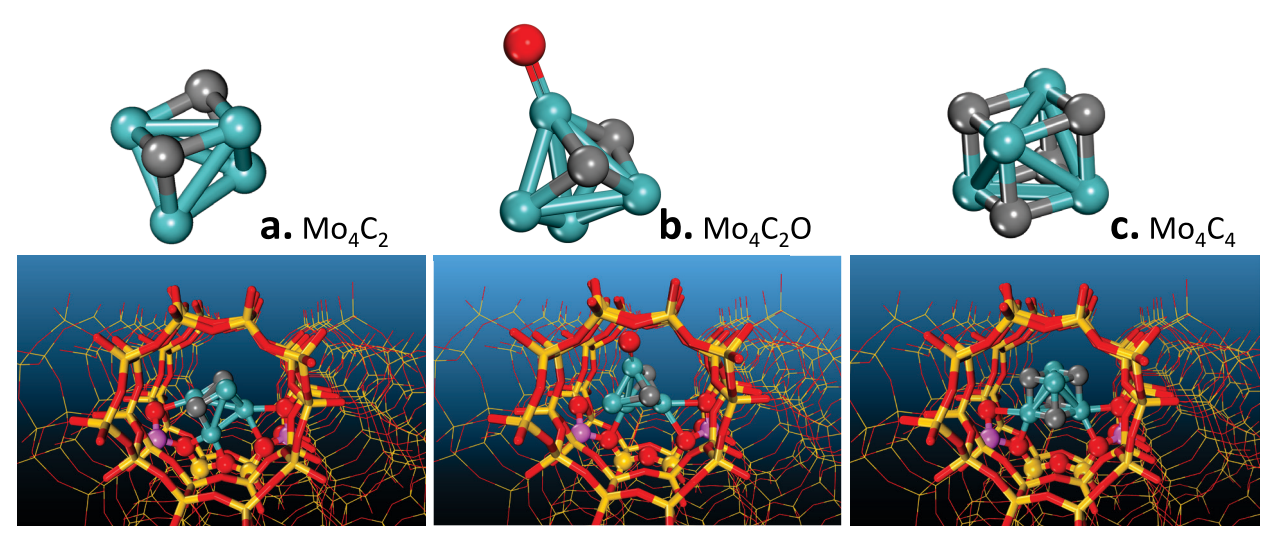


Figure 1. Structures of (a) Mo_4C_2 , a carbide with the Mo_2C stoichiometry, (b) Mo_4C_2O , an oxycarbide and (c) Mo_4C_4 , a carbide with excess carbon above the Mo_2C stoichiometry. Top row: isolated structures. Bottom row: same structures anchored on a double Al-atom framework site in the ZSM-5 zeolite.

Since a treatment with O2 can fully reverse agglomeration and convert Mo carbide nanoparticles into isolated Mo oxide nanostructures, it is likely that addition of an oxygencontaining molecule, such as CO2, into the reaction mixture with methane should partially change the composition of Mo nanostructures and slow the rate of their agglomeration, thus, serving as a means of controlling the dynamic composition, size and catalytic activity of Mo nanostructures. A similar effect can be expected when biomass-derived oxygen-containing hydrocarbons are co-fed with methane and when hydrodeoxygenation of biomass hydrocarbons is performed in the absence of methane. The effect of adding oxygen-containing molecules to the reaction mixture on the structure and catalytic properties of Mo species is not well understood. In addition, it is important to determine if it is preferable for catalytic performance to maintain Mo structures in a fully carbided MoC_x form or, in contrast, to convert them into an oxycarbide MoC_xO_y , an intermediate between an oxide and a carbide.

The current study addresses these issues by comparing the composition and size of Mo nanostructures for Mo/ZSM-5 catalysts with in situ X-ray absorption spectroscopic (XAS) measurements under three reaction conditions: (1) an O2 treatment, (2) reaction with only CH₄ and (3) reaction with a CH₄-CO₂ mixture. Additional experiments compare catalytic activities for CH₄ and CD₄ reaction feeds. The experimental results are complemented with density functional theory (DFT) calculations that identify Mo oxycarbide structures and evaluate structure-activity relationships by comparing methane activation mechanisms catalyzed by a Mo₄C₂ nanostructure (a carbide with the Mo₂C stoichiometry, Figure 1a), a Mo₄C₂O nanostructure (an oxycarbide with a single O atom, Figure 1b) and a Mo₄C₄ nanostructure (a carbide with excess carbon above the Mo₂C stoichiometry, Figure 1c) supported on ZSM-5 (Figure 2).

2. METHODS

2.1. Catalyst Synthesis. A ZSM-5 zeolite (Zeolyst International, CBV3024E, Si/Al = 15) was converted from the initial ammonium form to the hydrogen form (HZSM-5) by calcining in ambient air by ramping the temperature at 5 K/min to 875 K and holding at this temperature for 4 h. Mo was

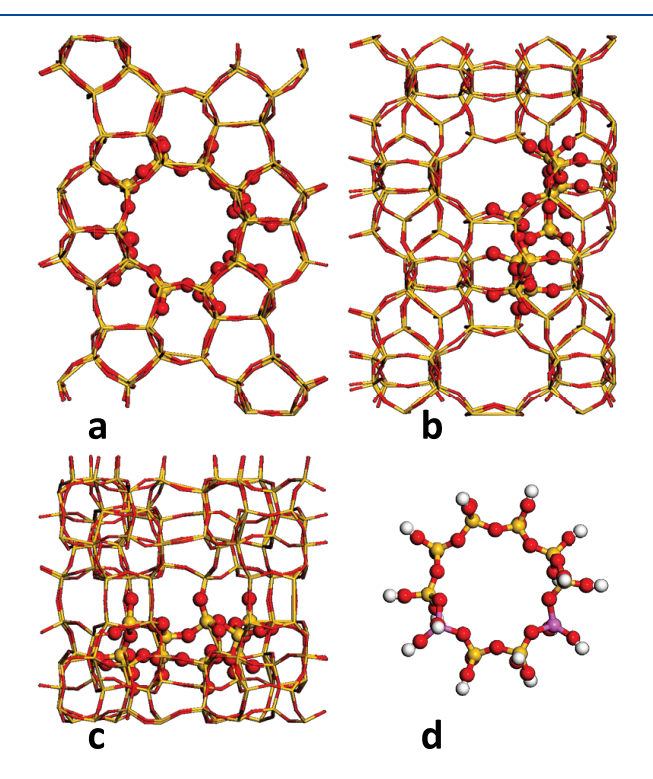


Figure 2. (a–c) Periodic and (d) cluster models of the ZSM-5 zeolite. Periodic model: (a) channel view, (b) side view and (c) top view. The periodic model has two full MFI unit cells ($Si_{192}O_{384}$) as a supercell. The 10-T ring treated as the quantum mechanical (QM) region is shown with a ball-and-stick representation. The rest of the periodic model treated as the molecular mechanical (MM) region is shown with a wireframe representation. (d) Cluster model of the same 10-T ring with the boundary O atoms terminated by H atoms. A double Alatom zeolite framework anchoring site is modeled by placing Al atoms into the T-8 and T-12 positions in the 10-T ring.

deposited onto the HZSM-5 support with the incipient wetness impregnation method using an aqueous solution of ammonium heptamolybdate tetrahydrate, $(NH_4)_6Mo_7O_{24}$ · $4H_2O$ (Alpha Aesar, 99.9%). Catalysts with two Mo loadings were prepared: 1.3 and 2.7 wt %. These Mo loading values are

Table 1. XANES and EXAFS Results for Mo Reference Compounds

		XANES	EXAFS		
reference compound	Mo oxidation state	K-edge energy (keV)	scatter	N	R (nm)
Mo foil	0	20.0000	Mo-Mo	8	0.27
$C_2H_5MoCO_3$	+1	20.0015			
$Mo_2(CH_3COO)_4$	+2	20.0037			
MoO_2	+4	20.0125			
MoO_3	+6	20.0167			
Na_2MoO_4	+6	20.0175	Mo=O	4	0.18
(NH ₄) ₆ Mo ₇ O ₂₄ ·6H ₂ O	+6	20.0167			

Table 2. XANES and EXAFS Results for Bulk Mo₂C and 2.7 wt % Mo/ZSM-5 Catalysts

	XANES	EXAFS		
catalyst	K-edge energy (keV)	scatter	N	R (nm)
Mo_2C	20.0018	Mo-C	9	0.21
		Mo-Mo	12	0.28
Mo/ZSM-5 in air flow at 773 K	20.0168	Mo=O	1.9	0.17
		Mo-O	2.0	0.21
Mo/ZSM-5 in 20 mol % CH ₄ /He flow at 973 K	20.0014	Mo-C	6.3	0.21
		Mo-Mo	2.7	0.30
Mo/ZSM-5 in 20 mol % $\rm CH_4/1$ mol % $\rm CO_2/He$ flow at 973 K	20.0141	Мо-О Мо-С	3.7	0.21
		Mo-Mo	1.7	0.30

based on the amount of Mo, not Mo oxide. After the impregnation, the catalysts were dried in ambient air at room temperature overnight and further by ramping the temperature at 1 K/min to 393 K and holding at this temperature for 5 h. After the drying, the catalysts were calcined in a 50 sccm flow of air (Airgas, Inc., ultrahigh purity) by ramping the temperature at 1 K/min to 773 K and holding at this temperature for 2 h. The same catalyst formulations were used in our previous studies. 1,15

2.2. In Situ X-ray Absorption Spectroscopy. In situ X-ray absorption spectra (XAS) were obtained using the insertion device beamline of the Materials Research Collaborative Access Team (10 ID, MRCAT) at the Advanced Photon Source, Argonne National Laboratory. Measurements were made in a quick-scan transmission mode (3.5 min) from 0.2500 keV below to 1.0000 keV above the Mo K-edge value of 20.0000 keV. The ionization chambers were optimized for the maximum current with a linear response (~10¹⁰ photons detected/s) with 10% absorption in the incident ion chamber and 70% absorption in the transmission detector. A Mo foil spectrum was simultaneously acquired with each measurement for energy calibration.

Reference compounds for Mo in different oxidation states were obtained from Sigma-Aldrich: Mo foil (\geq 99.9%), $C_2H_5MoCO_3$ (99%), $Mo_2(CH_3CO_2)_4$ (99%), MoO_2 (99%), MoO_3 (99%), Na_2MoO_4 (99%), and $(NH_4)_6Mo_7O_{24}\cdot 6H_2O$ (99%). Except for the Mo foil, the samples were diluted with SiO_2 , ground and pressed into self-supporting wafers. The reference Mo_2C bulk phase was synthesized in the X-ray absorption chamber from the ground and diluted MoO_2 by flowing a 20 mol % CH_4/H_2 gas mixture (both high-purity gases from Airgas) at 923 K for 2 h.

The Mo/ZSM-5 catalyst powder was pressed into a cylindrical sample holder with six wells as a self-supporting wafer. The sample wafer was treated in a quartz tube flow reactor (1 inch outer diameter, 10 inch length) equipped with Kapton windows and two Ultra-Torr fittings. Ball valves were welded to each Ultra-Torr fitting and served as the gas inlet

and outlet. An internal K-type thermocouple (Omega Engineering, Inc.) placed against the catalyst sample holder was used to monitor the catalyst temperature. The amount of a catalyst sample was adjusted to have an estimated absorbance of $\sim 1.0 \ \mu x$. Traces of oxygen and moisture in He were removed with a purifier (Matheson PUR-Gas Triple Purifier Cartridge). The catalyst was initially calcined in situ in an air flow (synthetic ultrazero grade air from Airgas) at 773 K for 3 h and analyzed after the calcination. After purging with He, the catalyst was exposed to a flow of a 20 mol % CH₄/He reaction mixture at 973 K for 3 h and analyzed again. Additionally, a separate catalyst sample was calcined and then exposed to a flow of a 20 mol % CH₄/He reaction mixture with an added 1 mol % CO2. In total, three measurements were collected for each catalyst (1.3 and 2.7 wt % Mo/ZSM-5): (1) after 3 h in air at 773 K, (2) after 3 h in 20 mol % CH₄/He at 973 K and (3) after 3 h in 20 mol % CH₄/1 mol % CO₂/He at 973 K. Spectra were obtained after cooling down to room temperature to minimize thermal effects. The K-edge energy of the XANES spectrum was determined from the inflection point in the leading edge, that is, the maximum in the first derivative of the leading edge. The experimental Mo-O and Mo-Mo phase shifts and backscattering amplitudes were obtained from the reference compound Na₂MoO₄ (Table 1, 4 Mo=O bonds with a distance of 0.18 nm) and the Mo foil (Table 1, 8 Mo-Mo bonds with a distance of 0.27 nm). Similarly, the phase and amplitude functions were obtained from the reference Mo₂C (Table 2, 9 Mo-C bonds with a distance of 0.21 nm and 12 Mo-Mo bonds with a distance of 0.27 nm). These reference results were used in analyzing the Mo/ZSM-5 measurements. Data normalization and background subtraction were performed using the WinXAS 3.2 software package. The coordination parameters were obtained using the least-squared error fit in the R-space of the nearest neighbor, k^2 -weighted Fourier transform data.

2.3. CH₄/CD₄ Temperature Programmed Reaction. In each test, a 0.03 g sample of the 1.3 wt % Mo/ZSM-5 catalyst was loaded in a U-shaped quartz tube using quartz wool as

bedding and placed in an Altamira AMI-200 instrument equipped with an oven and multiple mass flow controllers. The catalyst was initially calcined in a 30 sccm flow of 10 mol % O₂/Ar (Airgas, Inc., 10.00% Certified Mixture) by increasing the temperature at a ramp rate of 10 K/min to 773 K and holding at this temperature for 2 h. Then, the catalyst was purged with a 30 sccm flow of Ar (Airgas, Inc., ultrahigh purity) at 773 K for 30 min. After the Ar purge, the temperature programmed reaction was performed by introducing a 30 sccm flow of either 5 mol % CH₄ (Airgas, Inc., 99.999%) or 5 mol % CD₄ (Matheson, methane- d_4 , >99%) in Ar (Airgas, Inc., ultrahigh purity) and increasing the temperature from 773 to 1073 K with a ramp rate of 1 K/min. Reaction products were analyzed online with a Dycor Dymaxion DM100MS mass spectrometer by monitoring the following mass/charge (m/z) ratios: 2 (H_2) , 15 and 16 (CH_4) , 27 (C₂H₄), 29 and 30 (C₂H₆), 77 and 78 (C₆H₆) for the CH₄ feed; 4 (D₂), 18 and 20 (CD₄), 30 and 32 (C₂D₄), 34 and 36 (C_2D_6) , 82 and 84 (C_6D_6) for the CD_4 feed; 28 (CO), 20 and 40 (Ar), 44 (CO_2) for both feeds.

2.4. Computational Methods. Our previous spectroscopic and computational studies identified three types of zeolite anchoring sites: double Al-atom zeolite framework sites, single Al-atom zeolite framework sites and Si sites on the external surface of the zeolite. 1,15,24 Catalytic activities in methane activation with the formation of CH3 and H surface species were found to be similar for a Mo₄C₂ structure anchored on single and double Al-atom framework sites and significantly lower when this Mo carbide structure was anchored on Si sites on the external surface of the zeolite. In this work, catalytic activities in methane activation were compared with transition state calculations for three structures (top row of Figure 1): (a) a Mo₄C₂ carbide particle with the stoichiometry of a bulk β -Mo₂C carbide (C to Mo ratio of 1 to 2), (b) a Mo₄C₂O oxycarbide particle obtained by adding an oxygen atom to the Mo₄C₂ carbide particle and (c) a Mo₄C₄ carbide particle with excess carbon above the Mo₂C stoichiometry. All Mo particles were anchored on the same double Al-atom zeolite framework site (bottom row of Figure 1).

The optimized structure of an isolated Mo₄C₂O oxycarbide particle was obtained using a genetic algorithm by generating and analyzing multiple geometric structure permutations. First, a population of 32 candidate structures was generated and evaluated with DFT geometry optimization calculations. Then, a new generation of 32 "child" structures was created by combining portions of the initial "parent" population. The parent structures were selected on the basis of their fitness, which, in this case, was their total DFT energy. As a result, lower-energy structures were more likely to be selected to pass their characteristics to future generations. New child population structures were created with two methods: mutation and mating (also known as crossover). In the mutation method, Cartesian coordinates of an atom (x, y) and z) were modified randomly with a preset probability of 10%. In the mating method, two parent structures were selected to create two new child structures. A random plane passing through the center of mass of each parent structure was generated, and child structures were generated by selecting the atoms above the plane in one of the parents and below the plane in the other. In addition, a half of each child cluster was rotated through a random angle. Furthermore, seven variant crossover operations were used to generate additional child

population structures. For each pair of parents, a crossover operator was chosen randomly, ensuring a diverse population. Moreover, a "taboo" algorithm was employed that prevented generation of the same child structures in two consecutive generations, which further ensured the diversity of the population. After generation of a complete set of 32 child structures, the fitness of each new structure was computed, and a subsequent population of 32 child structures was created. The process continued until convergence was achieved. Evaluation of populations larger than 32 structures for several Mo carbide compositions showed no significant improvements in convergence. The probability of selecting a parent structure was proportional to its relative energy. During the first few generations, however, high-energy structures were assigned a higher probability than would be determined by their energy. This prevented the algorithm from converging to a local minimum. The likelihood of premature convergence was further minimized by employing a sliding scale factor for crossover probabilities. The convergence criterion was set as an energy change of less than 0.26255 kJ/mol (10⁻⁴ Ha) for 25 consecutive generations. After identifying five isolated Mo₄C₂O structures with lowest energies, their stabilities on the double Al-atom zeolite framework anchoring site were evaluated to confirm that the isolated Mo₄C₂O structure with the lowest energy remained the most energetically preferable structure after the zeolite anchoring (Figure 1b).

Gradient-corrected spin-polarized DFT calculations were performed using the DMol 3 code in the Materials Studio 6.1 software by BIOVIA Corporation. The calculations used the DNP basis set (version 3.5) and the GGA RPBE functional. Tightly bound core electrons of Mo atoms were represented with semicore pseudopotentials. Reciprocal-space integration over the Brillouin zone was approximated through Γ -point sampling (1 × 1 × 1 Monkhorst–Pack grid). The density mixing fraction of 0.2 with direct inversion in the iterative subspace (DIIS, size 6) and orbital occupancy with smearing of 0.005 Ha were used. The orbital cutoff distance was set at 0.44 nm for all atoms. These computational settings were successfully used by us previously for modeling Mo and Cr oxide and carbide structures.

The transition state calculations were performed in two stages. In the first stage, a 10-T cluster (Al₂Si₈O₃₀H₂₀) was used as the zeolite model (Figure 2d). In the second stage, the reaction pathways obtained with the 10-T cluster were refined with the same 10-T cluster embedded into the full periodic MFI structure (Figure 2a-c) using hybrid quantum mechanical and molecular mechanical (QM/MM) calculations. The cluster was generated from a 10-T ring of the sinusoidal channel of an MFI unit cell (96 Si and 192 O atoms) with the lattice constants of a = 2.0022, b = 1.9899 and c = 1.3383 nm. The dangling bonds of the boundary O atoms in the cluster were saturated by H atoms. To minimize cluster boundary effects and better simulate the overall zeolite structure, the coordinates of these terminal OH groups were constrained. The terminal O atoms were constrained at their original positions in the MFI unit cell. The terminal H atoms were constrained at the positions obtained with the following twostep procedure. First, the bonding Si atoms from the part of the zeolite framework that was cut out from the cluster were changed into H atoms. Second, the distance between the bonding O atoms in the cluster and the terminal H atoms was adjusted to 0.095 nm. Except for the terminal OH groups, the positions of all other cluster atoms and all atoms in the

anchored Mo carbide and oxycarbide structures as well as CH₄ were optimized. A double Al-atom zeolite framework anchoring site was modeled by placing one Al atom into the T-8 framework position and another Al atom into the T-12 position in the 10-T ring (Figure 2d). The Mo carbide and oxycarbide particles were anchored by replacing two H counterions in this double Al-atom framework anchoring site.

Transition state searches were performed in three phases. In the first phase, calculations with constrained optimization were performed by gradually changing the Mo-CH₄ and CH₃-H distances for the forward reaction: $CH_4 + 2^* = CH_3^* + H^*$. In the second phase, similar calculations with constrained optimization were repeated for the reverse reaction. In the final third phase, the energetically preferable reaction pathways identified with the constrained optimization calculations were refined using a combination of linear synchronous transit (LST) and quadratic synchronous transit (QST) algorithms with conjugate gradient refinement. After obtaining reaction pathway estimates with this three-phase procedure for the 10-T cluster zeolite model (Figure 2d), the results were further refined with the same procedure using the full periodic zeolite model. The same 10-T cluster was selected in the middle of two full MFI unit cells with $96 \times 2 = 192$ Si and $192 \times 2 = 384$ O atoms (Figure 2a-c). These two MFI unit cells were combined into a periodic supercell. The 10-T cluster and the boundary O atoms, which are shown in Figure 2a-c with a ball-and-stick representation, were treated as the DFT (QM) region, and the rest of the MFI supercell, shown in the same figure with a wireframe representation, was treated as the MM region. The QM region was embedded using mechanical embedding, with the total energy being calculated with a subtractive scheme. The QM/MM calculations used the same DFT settings as those employed in cluster calculations performed with DFT only. The MM calculations were performed with the GULP program in the Materials Studio QMERA module using the hybrid internal coordinate (HDLC) optimization method and the universal force field (UFF). The 10-T DFT region was in the middle of the periodic structure. Positions of all atoms in the zeolite framework were optimized during the calculations. Reaction energies are reported at 0 K without zero-point vibrational energy corrections using as a reference the initial reactant configuration: a gas-phase CH₄ molecule at a distance of ~0.4 nm from the evaluated zeolite-supported Mo carbide or oxycarbide structure.

3. RESULTS

3.1. XANES/EXAFS. The Mo K-edge energies obtained from X-ray absorption near-edge structure (XANES) spectra of the reference Mo compounds gradually increase with increasing formal Mo oxidation state (Table 1): from 20.0000 keV for Mo(0) in the Mo foil to 20.0015 keV for Mo(+1) in $C_2H_5MoCO_3$, 20.0037 keV for Mo(+2) in Mo₂(CH₃COO)₄, 20.0125 keV for Mo(+4) in the bulk MoO₂ and, finally, 20.0167-20.0175 keV for Mo(+6) in the bulk MoO₃, Na₂MoO₄ and (NH₄)₆Mo₇O₂₄·6H₂O. The dependence of the Mo K-edge energy values on the Mo oxidation state in Figure 3 exhibits a linear correlation. This correlation obtained with the reference Mo compounds was used for evaluating the state of Mo in the Mo/ZSM-5 catalysts after the calcination in air prior to the reactions as well as under the reaction conditions with CH₄/He and CH₄/CO₂/ He.

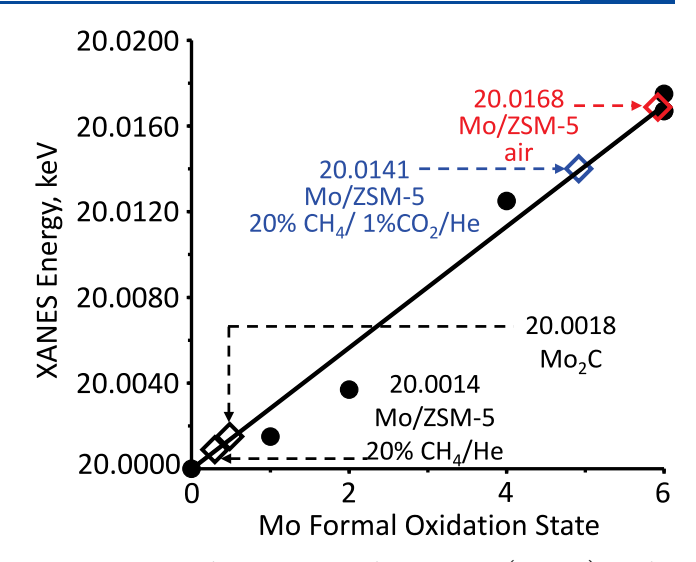


Figure 3. X-ray absorption near-edge structure (XANES) K-edge energies for Mo reference compound as a function of the Mo formal oxidation state (filled symbols) exhibit a linear correlation. The obtained correlation is compared with in situ results for the 2.7 wt % Mo/ZSM-5 catalyst under various reaction conditions (open symbols).

A comparison of the in situ XANES spectra of the Mo Kedge for the 2.7 wt % Mo/ZSM-5 (Si/Al = 15) catalyst after the calcination in air at 773 K and the reference bulk MoO $_3$ in Figure 4a shows that these spectra are similar. The Mo Kedge energy of 20.0168 keV for the 2.7 wt % Mo/ZSM-5 catalyst in air (Table 2, same value for the 1.3 wt % Mo/ZSM-5) is close to the value of 20.0167 keV for the bulk MoO $_3$ (Table 1). The shapes of these spectra are also similar (Figure 4a), confirming that Mo supported on ZSM-5 after calcination is in its highest oxidation state of +6 and is present in the form of Mo oxide structures. This result is in agreement with our previous analysis of in situ ultraviolet—visible (UV—vis) spectra. 1,15

After 3 h in a flow of 20 mol % CH_4/He at 973 K, when Mo/ZSM-5 serves as a dehydroaromatization catalyst, the in situ XANES spectrum becomes different than that for the initial catalyst in air and similar to that of the reference bulk Mo₂C carbide (Figure 4b). The Mo K-edge energy for the 2.7 wt % Mo/ZSM-5 shifts down from 20.0168 to 20.0014 keV (20.0016 keV for the 1.3 wt % Mo/ZSM-5), close to the value of 20.0018 keV for the Mo₂C carbide (Table 2). This result demonstrates that under the reaction conditions with methane, the initial zeolite-supported Mo oxide structures transform into Mo carbide structures.

When a small amount of $\rm CO_2$ is added to the reaction feed mixture (1 mol % $\rm CO_2$ in 20 mol % $\rm CH_4/He$) at 973 K, the XANES spectrum also changes, but in this case, it becomes intermediate between those for the initial Mo/ZSM-5 in air and the catalyst under the reaction conditions with methane only (Figure 4c). The Mo K-edge energy changes to 20.0141 keV for the 2.7 wt % Mo/ZSM-5 (20.0154 keV for the 1.3 wt % Mo/ZSM-5), which is between the values of 20.0168 keV for Mo(+6) oxide structures in the initial catalyst after the calcination in air and 20.0014 keV for Mo carbide structures under the reaction conditions with methane only (Table 2 and Figure 3). These results demonstrate that $\rm CO_2$ addition prevents the full transformation of the initial Mo oxide structures into a Mo carbide and, instead, causes the formation of Mo oxycarbide structures with an intermediate stoichiom-

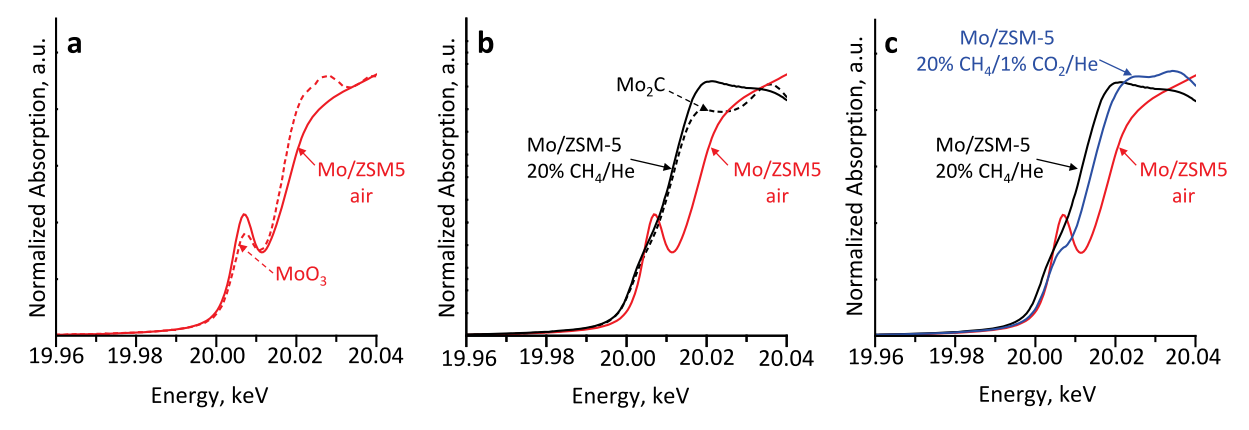


Figure 4. In situ XANES K-edge spectra for the 2.7 wt % Mo/ZSM-5 catalyst under various reaction conditions are compared to calibration results for reference compounds. (a) The spectrum of Mo/ZSM-5 after 3 h in air at 773 K is similar to that of the bulk MoO₃. (b) The spectrum of Mo/ZSM-5 after 3 h in 20 mol % CH_4/He at 973 K is different from that collected in air and similar to that of the bulk Mo₂C. (c) The spectrum of Mo/ZSM-5 after 3 h in 20 mol % $CH_4/1$ mol % CO_2/He at 973 K is intermediate between the spectra for the same catalyst in air and in CH_4 without CO_2 .

etry of MoC_xO_y . Since the catalyst bed is uniform, the formation of a mixture of a Mo oxide phase at the beginning of the bed and a Mo carbide phase at the end of the bed, which would also produce an intermediate overall stoichiometry, can be ruled out.

The in situ extended X-ray absorption fine structure (EXAFS) results in Table 2 provide information on the radial distribution of atoms around a Mo atom. The EXAFS spectrum for the 2.7 wt % Mo/ZSM-5 after calcination in air with two k^2 -weighted Fourier transform magnitude peaks indicates the presence of two neighboring O atoms at 0.17 and 0.21 nm. The first O atom at 0.17 nm is assigned to Mo=O double bonds based on the calibration with the Na2MoO4 reference compound, in which Mo and O atoms are arranged in tetrahedron $(Mo=O_4)^{2-}$ structures with a bond distance of 0.18 nm (Table 1). The second peak at a larger bond length of 0.21 nm must be from Mo-O single bonds. The coordination numbers for both oxygen types are close to 2 (Table 2). No neighboring atoms at a distance of about 0.3 nm characteristic of Mo-Mo bonds (Table 1) are detected and, therefore, a Mo atom does not have other Mo atoms in its coordination shell. Similar results were obtained for the 1.3 wt % Mo/ZSM-5. Consequently, the Mo oxide structures are isolated and have only a single Mo atom with a total of four bonded O atoms. These results are consistent with our previously reported identification of Mo oxide structures after calcination as isolated dioxo species with a single Mo atom.

Under the reaction conditions with CH₄/He, the EXAFS peak at 0.17 nm for Mo=O bonds disappears, the peak at 0.21 nm increases, and a new peak at 0.30 nm is observed for the 2.7 wt % Mo/ZSM-5 (Table 2). The disappearance of the Mo=O bonds confirms that the initial Mo oxide structures are no longer present. The new peak at 0.30 nm is assigned to Mo-Mo bonds based on the calibration with the Mo foil (0.27 nm, Table 1) and the bulk Mo₂C (0.28 nm, Table 2). The appearance of Mo-Mo bonds indicates agglomeration of the initial structures with a single Mo atom. Based on the similarity of the XANES spectra for the 2.7 wt % Mo/ZSM-5 and bulk Mo₂C (Figure 4b), the peak at 0.21 nm in this case is assigned to Mo-C bonds based on the calibration with the bulk Mo₂C (Table 2). The intensity of the peak at 0.30 nm is substantially lower than that for the bulk Mo₂C, indicating that a Mo atom has significantly fewer than 12 Mo atom neighbors present in the bulk Mo_2C . The average number of neighbors for the Mo atom is estimated to be 2.7 Mo atoms and 6.3 C atoms (Table 2). These values correspond to an average stoichiometry of $Mo_{3.7}C_{6.3}$ for the 2.7 wt % Mo/ZSM-5. For the lower loading 1.3 wt % Mo/ZSM-5, Mo-Mo bonds are not detected, and an average stoichiometry of $MoC_{2.2}$ is estimated. These results indicate that the transformation from oxide to carbide structures proceeds prior to agglomeration and that a greater separation of Mo atoms on the support at the lower Mo loading decreases the agglomeration rate. The amount of carbon in the carbide structures for both Mo loadings is above the 1 to 2 ratio of C to Mo in the orthorhombic β - Mo_2C and, furthermore, above the equimolar ratio in the hexagonal α -MoC and cubic δ -MoC.

After the addition of 1% CO $_2$ to the 20% CH $_4$ /He feed, the intensity of the EXAFS peak at 0.30 nm for the Mo–Mo bonds decreases relative to that under the reaction conditions with only methane for the 2.7 wt % Mo/ZSM-5. The estimated number of Mo neighboring atoms declines from 2.7 to 1.7 (Table 2), demonstrating that CO $_2$ addition not only changes the composition of the Mo structures into an oxycarbide (Figure 3) but also slows their agglomeration.

3.2. CH₄/CD₄ Temperature Programmed Reaction. Mass spectrometer signals as a function of temperature, which was increased with a ramp rate of 1 K/min, for the reactions with CH₄ and CD₄ over the 1.3 wt % Mo/ZSM-5 are compared in Figure 5. Below 890 K, CH₄ is consumed but without benzene formation, indicating an induction period when the initial Mo oxide structures become carbided (Figure 5a). During this induction period, CO₂ and H₂O as well as small amounts of H₂ and C₂H₄ are observed as the reaction products, in agreement with previous studies. 1,20,22,25 Above 890 K, the rate of CH₄ consumption changes, and both benzene and hydrogen are observed as the main products, indicating the onset of the dehydroaromatization reaction. In contrast, the onset of the dehydroaromatization reaction with CD₄ is observed at a much higher temperature of 1042 K (Figure 5b). This large temperature difference demonstrates a much slower reaction rate with CD₄ and, therefore, suggests a primary H/D kinetic isotope effect when an H atom in CH₄ is involved in the rate determining step. The isotope results, thus, indicate that CH₄ activation with the splitting of the first C-H bond over Mo structures is rate determining. The same

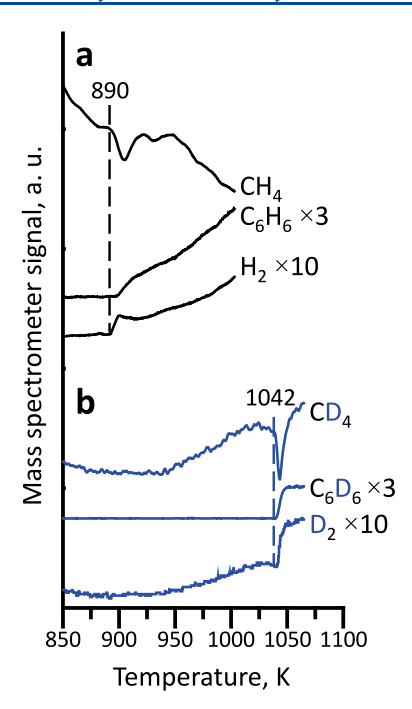


Figure 5. Results of temperature programmed reactions for 1.3 wt % Mo/ZSM-5 with (a) CH₄ and (b) CD₄.

conclusion was proposed based on a comparison of reaction results for calcined zeolite-supported Mo catalysts, which had an induction period, and the corresponding precarbided catalysts, which did not have an induction period.

3.3. Identification of Mo₄C₂O Structures. The optimized geometries of Mo₄C₂ and Mo₄C₄ carbide structures (Figure 1a,c) were obtained using a genetic algorithm and reported previously.¹⁵ For identifying the lowest-energy Mo₄C₂O oxycarbide structure, the same genetic algorithm was employed based on an adaptation of the principle of Darwinian evolution, in which the more fit individuals are more likely to pass their characteristics to future generations. The obtained five lowest-energy Mo₄C₂O structures are shown in Figure 6, and their geometries are provided in Tables S1-S5. In the most stable structure (Figures 1b and 6a), the O

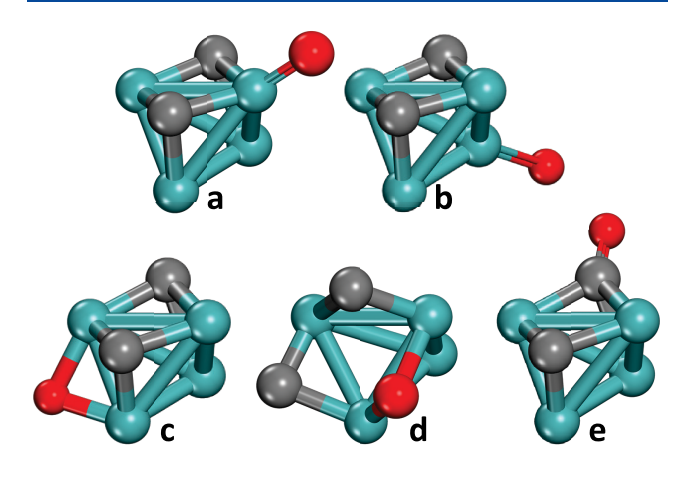


Figure 6. Mo₄C₂O oxycarbide structures identified with the genetic algorithm. Structure (a) is the most stable one. Structures (b)-(e) are progressively less stable by 14, 54, 71 and 71 kJ/mol, respectively. Geometry details with bond length and angles for these structures are provided in Tables S1-S5.

atom is terminally bound with a double bond to a single Mo atom with two neighboring C atoms. This structure is more stable by 14 kJ/mol than the structure where the O atom binds to a Mo atom with only one neighboring C atom (Figure 6b) and by 54 kJ/mol than the structure where the O atom binds to two Mo atoms in a bridge position (Figure 6c). The structures with the O atom binding to another pair of Mo atoms in a bridge position (Figure 6d) or to a single C atom (Figure 6e) are even less stable.

Our previous DFT calculations confirmed that the most stable isolated Mo_xC_v carbide structures remain the most stable after anchoring on the zeolite sites. 15 In this work, the same was confirmed for the Mo₄C₂O oxycarbide. The most stable isolated Mo₄C₂O structure (Figure 6a) remains the most stable after anchoring on a double Al-atom zeolite framework site (Figure 1b). The less stable Mo₄C₂O structures in Figure 6b-e remain less stable by 16-76 kJ/mol after anchoring on the same site. The zeolite in these calculations was modeled with the full periodic structure (Figure 2a-c).

3.4. Methane Activation over Mo₄C₂, Mo₄C₂O and Mo_4C_4 . The effect of the catalyst structure on the catalytic activity was evaluated with transition state DFT calculations for methane activation: splitting of the first C-H bond with the formation of CH₃ and H surface species, which is the likely rate determining step based on the CH₄/CD₄ results in Figure 5. The calculations were performed with the zeolite-anchored Mo₄C₂, Mo₄C₂O and Mo₄C₄ structures using the two adjacent full ZSM-5 unit cells as a periodic supercell (Figure 1a-c). For the Mo₄C₂ carbide (Figure 7), as methane approaches the Mo particle, the C atom in methane begins to interact with a Mo atom that is not directly bonded to the zeolite (Figure 7b). At the same time, one of the H atoms begins to be stabilized by a C atom in the carbide, and the bond distance between this H atom and the C atom in methane gradually increases (Table S6). In the transition state, methane forms a $C-H-CH_3-Mo$ cycle on the Mo-C pair of atoms, which serves as a single active site ($E_a = 112 \text{ kJ/mol}$, Figure 7c and Table S6). The Mo-C site activates methane in a scissoring motion: the C-H bond length in methane gradually increases as the H atom becomes bonded to the carbide C atom and the CH₃ fragment becomes bonded to the carbide Mo atom (Figure 7d,e and Table S6).

Compared to the Mo₄C₂ carbide, the presence of oxygen in the Mo₄C₂O oxycarbide can affect methane activation on a Mo-C site and can also open a new reaction pathway on a Mo-O site. Both effects were evaluated. When methane is activated on a Mo-C site (Figure 8), the O atom moves to a bridge-bonding position between two Mo atoms with a low activation energy, and the C-H bond splitting in methane proceeds through the same scissoring motion as without oxygen. The H atom gradually binds to the oxycarbide C atom as the CH3 fragments binds to the oxycarbide Mo atom. The geometry of the transition state with the C-H-CH₃-Mo cycle and the activation energy are practically unaffected by the oxygen presence (Figure 8c and Table S7). When methane is activated on a Mo-O site (Figure 9), the initial structure is identical with methane first establishing a bond with the Mo atom and forcing the O atom bonded to this Mo atom to move closer to a Mo-Mo bridging position (Figures 8b and 9b). However, the subsequent steps are energetically different. Importantly, the O-H bond distance of 0.12 nm in the transition state cycle O-H-CH₃-Mo (Figure 9c and Table S8) is shorter than the C-H bond distance of 0.15 nm in the

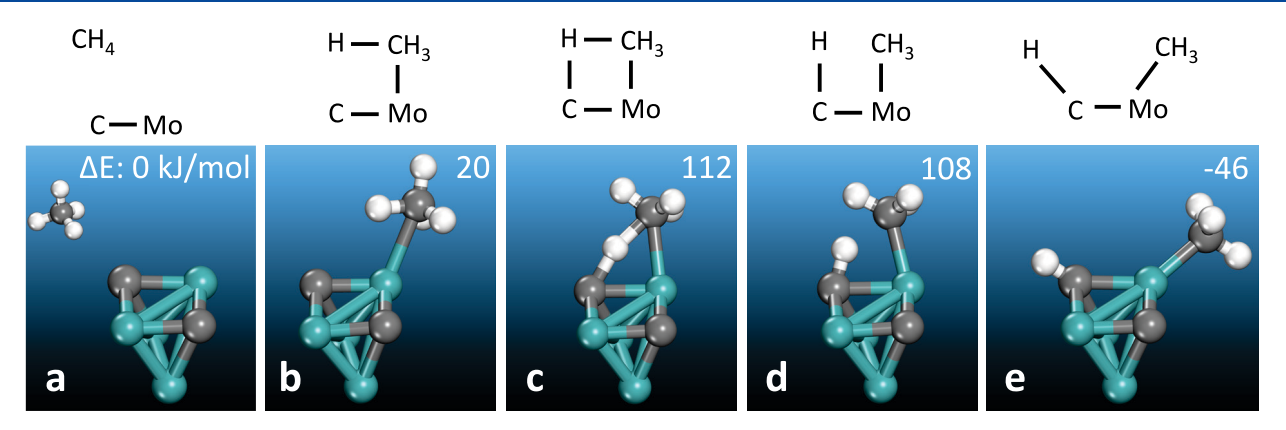


Figure 7. Methane activation $(CH_4 + 2^* = CH_3^* + H^*)$ over the Mo_4C_2 carbide structure anchored in the zeolite framework (Figure 1a). Only the Mo_4C_2 carbide without the zeolite framework is shown for clarity. Each frame shows the reaction energy relative to gas-phase methane. Reaction pathway: (a) CH_4 above the active site, (b) the C atom in CH_4 starts bonding to a Mo atom, (c) transition state with a $C-H-CH_3-Mo$ cycle on a Mo-C pair of atoms in the Mo_4C_2 carbide that acts as a single active site, (d) CH_3 and H surface fragments begin to form and (e) CH_3 and CH_4 fragments bonded correspondingly to the CH_4 atoms of the active site. Geometry details with bond lengths for these five structures are provided in Table S6.

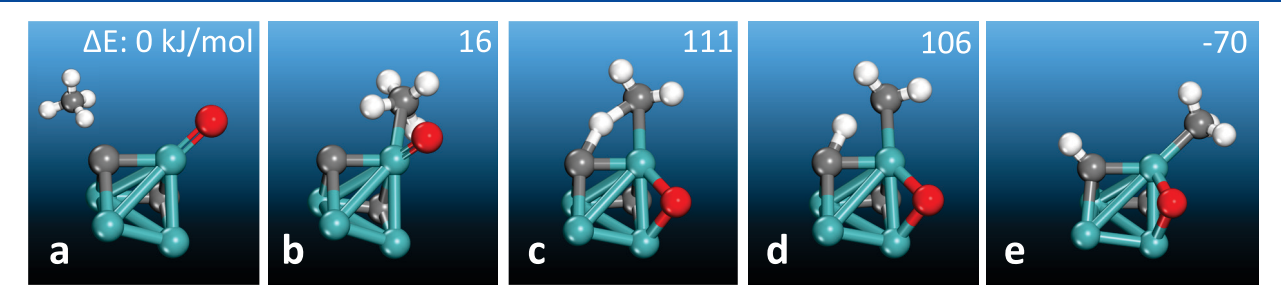


Figure 8. Methane activation ($CH_4 + 2^* = CH_3^* + H^*$) over the Mo_4C_2O oxycarbide structure anchored in the zeolite framework (Figure 1b). Mo-C active site. Only the Mo_4C_2O oxycarbide without the zeolite framework is shown for clarity. Each frame shows the reaction energy relative to gas-phase methane. Reaction pathway: (a) CH_4 above the active site, (b) the C atom in CH_4 starts bonding to a Mo atom, (c) transition state with a $C-H-CH_3-Mo$ cycle on a Mo-C pair of atoms in the Mo_4C_2O oxycarbide that acts as a single active site, (d) CH_3 and H surface fragments begin to form and (e) CH_3 and H fragments bonded correspondingly to the Mo and C atoms of the active site. Geometry details with bond lengths for these five structures are provided in Table S7.

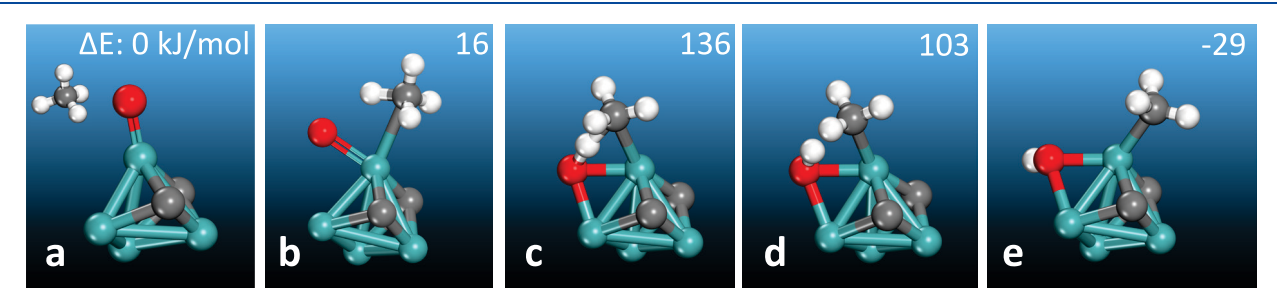


Figure 9. Methane activation $(CH_4 + 2^* = CH_3^* + H^*)$ over the Mo_4C_2O oxycarbide structure anchored in the zeolite framework (Figure 1b). Mo-O active site. Only the Mo_4C_2O oxycarbide without the zeolite framework is shown for clarity. Each frame shows the reaction energy relative to gas-phase methane. Reaction pathway: (a) CH_4 above the active site, (b) the C atom in CH_4 starts bonding to a Mo atom, (c) transition state with an $O-H-CH_3-Mo$ cycle on a Mo-O pair of atoms in the Mo_4C_2O oxycarbide that acts as a single active site, (d) CH_3 and H surface fragments begin to form and (e) CH_3 and H fragments bonded correspondingly to the Mo and O atoms of the active site. Geometry details with bond lengths for these five structures are provided in Table S8.

analogous C-H-CH₃-Mo cycle (Figure 8c and Table S7), resulting in a higher activation energy of 136 kJ/mol (Figure 9c). Consistently with the higher activation energy, the CH₃ and H surface species formed after methane activation are less stable on the Mo-O site (-29 kJ/mol, Figure 9e) than on the Mo-C site (-70 kJ/mol, Figure 8e). The calculations, therefore, suggest that the Mo-O site is less catalytically active than the Mo-C site.

When methane is activated on the Mo_4C_4 carbide (Figure 10), the geometry and energy of the transition state C-H-

 ${
m CH_3-Mo}$ cycle (Figure 10c and Table S9) are similar to those on the ${
m Mo_4C_2}$ carbide (Figure 7c and Table S6). The calculations, therefore, suggest that the extra carbon in the ${
m Mo_4C_4}$ carbide does not change the methane activation mechanism and has practically no effect on the catalytic activity.

4. DISCUSSION

The XANES and EXAFS results demonstrate that after calcination in air, Mo is present in its highest oxidation state

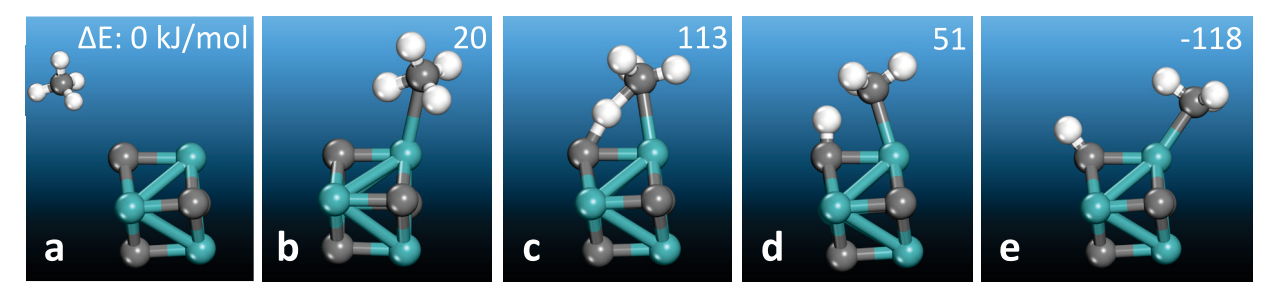


Figure 10. Methane activation ($CH_4 + 2^* = CH_3^* + H^*$) over the Mo_4C_4 carbide structure anchored in the zeolite framework (Figure 1c). Only the Mo_4C_4 carbide without the zeolite framework is shown for clarity. Each frame shows the reaction energy relative to gas-phase methane. Reaction pathway: (a) CH_4 above the active site, (b) the C atom in CH_4 starts bonding to a Mo atom, (c) transition state with a $C-H-CH_3-Mo$ cycle on a Mo-C pair of atoms in the Mo_4C_4 carbide that acts as a single active site, (d) CH_3 and H surface fragments begin to form and (e) CH_3 and H fragments bonded correspondingly to the Mo and C atoms of the active site. Geometry details with bond lengths for these five structures are provided in Table S9.

of +6 as isolated oxide structures on the zeolite support (Figures 3 and 4a). The oxide structures have a single Mo atom that is bonded to two O atoms with a short bond distance of 0.17 nm (Mo=O bonds) and additional two O atoms with a longer bond distance of 0.21 nm (Mo-O bonds) (Table 2). These results confirm our previously reported identification of the oxide structures as isolated $Mo(=O)_2^{2+}$ dioxo species anchored on a double Al-atom zeolite framework site (Figure 11a). The identification was made by analyzing in

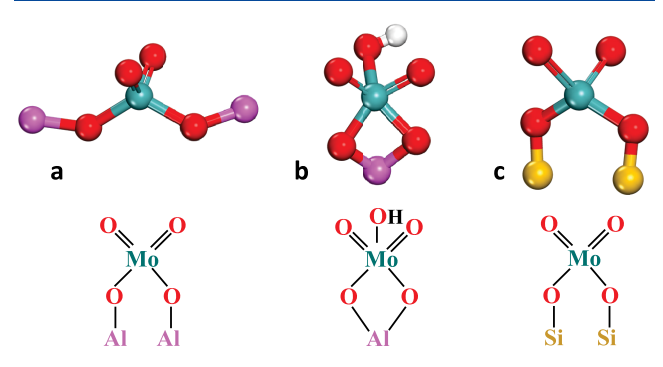


Figure 11. Mo oxide structures: (a) $Mo(=O)_2^{2+}$ dioxo species anchored on a double Al-atom zeolite framework site, (b) $Mo(=O)_2OH^+$ dioxo species anchored on a single Al-atom zeolite framework site and (c) $(Si-O-)_2Mo(=O)_2$ dioxo species on the external surface of the zeolite.

situ UV-vis and operando Raman spectroscopic results with DFT calculations. The DFT calculations show that two terminal O atoms are bonded to a single Mo with a short bond distance of 0.17 nm and additionally bonded to two zeolite framework O atoms with a longer distance of 0.21 nm (Figure 11a). Changes in the operando Raman spectra during catalyst regeneration with gas-phase O2 and in situ infrared (IR) spectra in the OH vibrational region for ZSM-5 before and after Mo deposition show that double Al-atom sites in the zeolite framework are preferable for anchoring Mo oxide structures, and these sites are preferentially populated first. Afterward, single Al-atom anchoring sites become populated (Figure 11b), followed by Si sites on the external surface of the zeolite (Figure 11c). 1,15 The same zeolite anchoring sites were confirmed with spectroscopic and computational studies for Cr oxide structures.²⁴ Single Al-atom anchoring sites become populated for catalysts with an increasing Mo loading at a constant Si/Al ratio in the zeolite. In addition, the fraction of Al atoms in single, rather than double, Al-atom sites increases

rapidly with increasing zeolite Si/Al ratio. ^{1,15} As there are fewer and fewer Al atoms in the zeolite unit cell, it is progressively less likely that two Al atoms are in proximity to each other and can serve as a double Al-atom anchoring site. For catalysts with an Al to Mo ratio of less than unity due to either a high Mo loading or a high Si/Al ratio, there is not a sufficient number of double or single Al-atom anchoring sites for each Mo atom, and the Mo oxide species are forced to anchor on Si sites on the external surface of the zeolite. For the 1.3 and 2.7 wt % Mo/ZSM-5 (Si/Al = 15) catalysts in the current study, the Al/Mo ratios are large at 7.0 and 3.5, respectively. Accordingly, most Mo oxide species were found to be anchored on double Al-atom zeolite framework sites (Figure 11a) based on spectroscopic measurements. ^{1,15}

A comparison of ZSM-5, TS-1 and other supports confirmed that framework Al sites in ZSM-5 stabilized dispersed Mo structures.²⁷ Decreasing the number of anchoring sites on the external surface of the zeolite by selective silanation improved catalyst selectivity and stability. ²⁸ In addition, previous studies suggest that carbided Mo structures formed under reaction conditions with methane remain mostly on the same Al anchoring sites in the zeolite framework as the initial Mo oxide structures. 1,15,29 Therefore, the carbided Mo structures are likely to remain anchored on double Al-atom anchoring sites. Furthermore, our previous computational results indicate that the catalytic activities of the Mo₄C₂ carbide structure in methane activation are similar when it is anchored on double and single Al-atom zeolite framework sites and lower for Si sites on the external surface of the zeolite. In this work, therefore, the effects of how the structure of Mo species affects their catalytic activity were evaluated only on double Al-atom zeolite framework sites (Figure 1).

Under reaction conditions with methane, two processes begin: the initial isolated Mo oxide structures become carbided and start to agglomerate. ^{19,20,25} Results of a recent study with operando X-ray methods show that the transformation is gradual: from the initial oxide to an oxycarbide and then to a carbide. ²² Operando Raman measurements with simultaneous monitoring of reaction products reveal that the only initial carbon-containing product of methane is CO₂, which must be a product of the Mo oxide converting into a carbide, and that aromatic products are not produced until the Mo oxide species are no longer observed spectroscopically. ¹ The XANES and EXAFS results in this work show that the conversion to a Mo carbide proceeds prior to agglomeration. The initial Mo oxide structures in the 1.3 wt % Mo/ZSM-5 catalyst convert to

carbide structures with an average stoichiometry of $MoC_{2.2}$ after 3 h in methane flow. Thus, no agglomeration was observed with Mo atoms remaining mostly isolated even after the complete transformation into a carbide and serving as a dehydroaromatization catalyst. A comparison with the 2.7 wt % Mo/ZSM-5 catalyst, for which the average stoichiometry is $Mo_{3.7}C_{6.3}$ under the same reaction conditions, demonstrates that the rate of agglomeration depends on the Mo loading and, as expected, increases for the higher Mo loading.

Our previous studies show that the agglomeration can be practically reversed by a treatment with gas-phase $\mathrm{O_2}^{.1}$ The results in this study show that the presence of an oxygencontaining molecule, such as $\mathrm{CO_2}$, in the methane reaction feed slows the Mo agglomeration process. In addition, the presence of $\mathrm{CO_2}$ changes the composition of Mo nanostructures. While the presence of $\mathrm{O_2}$ in the absence of methane reverses the agglomeration and regenerates the original isolated Mo oxide species, the presence of $\mathrm{CO_2}$ concurrently with methane only slows the agglomeration and changes the composition from a Mo carbide into a Mo oxycarbide.

DFT calculations show that zeolite-supported Mo carbide particles are not, strictly speaking, a pure carbide. They are nanostructures where Mo atoms are bonded to the zeolite through framework O atoms (Figure 1a,c). All computationally evaluated Mo_2C_x and Mo_4C_x particles anchor similarly. Therefore, there are some O atoms in the Mo coordination shell. However, in the presence of CO₂, the number of O atoms coordinated with Mo clearly increases based on the XAS measurements (Figures 3 and 4c), indicating the formation of an oxycarbide with O atoms bonded to Mo and not bonded to the support. It is, therefore, important to evaluate catalytic differences between a carbide and an oxycarbide. It is also important to evaluate the catalytic effect of the C to Mo ratio. Although the XANES results show the similarity of Mo/ZSM-5 to β -Mo₂C (Figure 4b), the EXAFS analysis suggests average stoichiometries of Mo_{3.7}C_{6.3} for the 2.7 wt % Mo and MoC_{2.2} for the 1.3 wt % Mo/ZSM-5 catalysts, indicating that the amount of carbon in the zeolite-supported Mo nanostructures is significantly higher than the 1 to 2 ratio of C to Mo.

The transition state calculations for the Mo₄C₂, Mo₄C₂O and Mo₄C₄ particles summarized in Figures 7-10 provide information on how the catalytic activity is affected by the presence of an oxygen atom and excess carbon. The calculations show that the reaction mechanism for methane activation over the Mo₄C₂ particle proceeds on a pair of Mo-C atoms, which serves as a single active site. Methane is activated with the formation of a CH3 surface fragment bound to the Mo atom and an H atom bound to the C atom of the active site (Figure 7). The presence of an O atom in the Mo₄C₂O oxycarbide practically does not affect the reaction mechanism and the activation energy when methane activation proceeds on a Mo-C active site. The transition state structures and energies for the Mo₄C₂ carbide in Figure 7 and for the Mo₄C₂O oxycarbide in Figure 8 are similar. In contrast, when methane is activated on a Mo-O active site, the transition state structures become different, and the activation energy increases (Figure 9). The computational results, therefore, suggest that a small amount of oxygen in a Mo oxycarbide particle does not affect methane activation if the reaction can proceed on a Mo-C active site. However, if the oxygen concentration of a Mo particle increases to a point when methane activation has to proceed on a Mo-O site, the catalytic activity is predicted to decline. This prediction is

consistent with experimentally observed higher catalyst stabilities in the presence of $\mathrm{CO_2}^{30-32}$ and an abrupt loss of catalytic activity when the $\mathrm{CO_2}$ to methane ratio exceeds $0.1.^{31}$ The computational results also suggest that, depending on the reactor type and the configuration of the catalyst bed, it may be beneficial to introduce an oxygen-containing molecule not directly with the hydrocarbon feed, but separately and gradually along the catalyst bed to avoid overoxidizing and converting the beginning of the bed into a Mo oxide phase, while the end of the bed remains fully carbided.

The similarities of the transition state structures and energies for the $\mathrm{Mo_4C_2}$ carbide in Figure 7 and the $\mathrm{Mo_4C_4}$ carbide in Figure 10 suggest that additional carbon does not affect methane activation as long as Mo atoms are accessible to methane and the reaction can proceed on a Mo–C active site. However, if the carbon concentration of a Mo nanostructure increases to a point when Mo atoms are covered by carbon and there are no Mo–C active sites accessible to methane, the catalytic activity is predicted to decline dramatically.

5. CONCLUSIONS

Depending on reaction conditions, the composition of supported Mo structures changes dynamically from an oxide to oxycarbide to carbide and in reverse. Under reaction conditions with methane in the absence of oxygen, initial isolated oxide structures with a single Mo atom convert into MoC_x carbide structures that gradually agglomerate into nanoparticles. The rate of agglomeration increases with the Mo loading. In contrast, under reaction conditions with methane in the presence of oxygen-containing CO_2 , the initial Mo oxide structures do not become fully carbided, but form MoC_xO_y oxycarbide nanostructures. In addition, the agglomeration rate decreases. These results are consistent with effects of a regeneration treatment with O_2 that reverses carburization and agglomeration, restoring the original isolated Mo oxide structures.

Methane activation proceeds on a pair of Mo–C atoms, which act as a single catalytic active site. Methane is activated by forming a CH_3 fragment bonded to the Mo atom and an H atom bonded to the C atom of the active site.

The amount of carbon in the carbided Mo structures is above the C to Mo molar ratio of 1, that is, above the stoichiometric ratios in β -Mo₂C, α -MoC or δ -MoC. The excess carbon does not influence the rate of methane activation as long as C atoms do not restrict access to Mo atoms by forming a partial or full overlayer.

A small oxygen concentration in a Mo oxycarbide does not change the rate of methane activation. For larger oxygen concentrations, however, the reaction rate is expected to decline because the concentration of Mo–C active sites declines, and methane activation proceeds on the Mo–O sites that are predicted to be less catalytically active than the Mo–C sites.

It is preferable to maintain catalytic Mo structures in the form of an oxycarbide because this phase slows undesirable coking and agglomeration and since the presence of a small number of oxygen atoms does not affect the rate of methane activation. Controlling the dynamic composition, size and catalytic activity of supported Mo structures and maintaining them in an oxycarbide form under hydrocarbon reaction conditions can be accomplished by co-feeding an oxygencontaining molecule, for example, CO₂ or an oxygenated hydrocarbon.

ASSOCIATED CONTENT

S Supporting Information

The Supporting Information is available free of charge on the ACS Publications website at DOI: 10.1021/acs.jpcc.9b05449.

The Mo oxycarbide structures in Figure 6 are shown with atom numbering labels in Figure S1 and their geometries are provided in Tables S1–S5. Bond distances and energies for the transition state structures in Figures 7-10 are provided in Tables S6–S9 (PDF)

AUTHOR INFORMATION

Corresponding Authors

*E-mail: jeffrey-t-miller@purdue.edu (J.T.M.).

*E-mail: iew0@lehigh.edu (I.E.W.).

*E-mail: Simon.Podkolzin@Stevens.edu (S.G.P.).

ORCID 6

Jeffrey T. Miller: 0000-0002-6269-0620 Israel E. Wachs: 0000-0001-5282-128X Simon G. Podkolzin: 0000-0002-9536-7176

Present Addresses

^LCummins, Inc., Columbus, Indiana 47201, United States. [#]Integrated Analytical Laboratories, Randolph, New Jersey 07869, United States.

Author Contributions

Y.Z. obtained the modeling results and prepared all experimental and modeling results for publication. Y.T. prepared the catalysts, conceived and obtained the reaction results, and coordinated the XAS experiments. J.R.G. obtained and analyzed the XAS results. J.G. obtained initial modeling results. J.T.M. conceived and supervised the XAS study. I.E.W. supervised the catalyst preparation and reaction experiments and conceived and coordinated the XAS experiments. S.G.P. conceived and supervised the modeling study, analyzed all the results and wrote the manuscript with contribution from all authors.

Notes

The authors declare no competing financial interest.

ACKNOWLEDGMENTS

The work in S.G.P.'s group at Stevens Institute of Technology was supported by National Science Foundation grant CBET-1133987. The DFT calculations were performed with the Materials Studio software provided by Dassault Systèmes BIOVIA Corporation under a collaborative research license. We thank Felix Hanke and Victor Milman at Dassault Systèmes BIOVIA Corporation for discussions on computational parameters. We thank George Fitzgerald at Universal Display Corporation for his help in the computational identification of the Mo oxycarbide structures. The work in I.E.W.'s group at Lehigh University was supported by National Science Foundation grant CBET-1134012.

REFERENCES

(1) Gao, J.; Zheng, Y.; Jehng, J.-M.; Tang, Y.; Wachs, I. E.; Podkolzin, S. G. Identification of Molybdenum Oxide Nanostructures on Zeolites for Natural Gas Conversion. *Science* **2015**, 348, 686–690. (2) Yao, S.; Zhang, X.; Zhou, W.; Gao, R.; Xu, W.; Ye, Y.; Lin, L.;

Wen, X.; Liu, P.; Chen, B.; et al. Atomic-Layered Au Clusters on α -MoC as Catalysts for the Low-Temperature Water-Gas Shift Reaction. *Science* **2017**, 357, 389–393.

- (3) Carrasquillo-Flores, R.; Ro, I.; Kumbhalkar, M. D.; Burt, S.; Carrero, C. A.; Alba-Rubio, A. C.; Miller, J. T.; Hermans, I.; Huber, G. W.; Dumesic, J. A. Reverse Water—Gas Shift on Interfacial Sites Formed by Deposition of Oxidized Molybdenum Moieties onto Gold Nanoparticles. *J. Am. Chem. Soc.* **2015**, *137*, 10317—10325.
- (4) Lin, L.; Zhou, W.; Gao, R.; Yao, S.; Zhang, X.; Xu, W.; Zheng, S.; Jiang, Z.; Yu, Q.; Li, Y.-W.; et al. Low-Temperature Hydrogen Production from Water and Methanol Using Pt/A-MoC Catalysts. *Nature* **2017**, *544*, 80–83.
- (5) Noh, H.; Cui, Y.; Peters, A. W.; Pahls, D. R.; Ortuño, M. A.; Vermeulen, N. A.; Cramer, C. J.; Gagliardi, L.; Hupp, J. T.; Farha, O. K. An Exceptionally Stable Metal—Organic Framework Supported Molybdenum(VI) Oxide Catalyst for Cyclohexene Epoxidation. *J. Am. Chem. Soc.* **2016**, *138*, 14720—14726.
- (6) Xu, C.; Wang, L.; Liu, Z.; Chen, L.; Guo, J.; Kang, N.; Ma, X.-L.; Cheng, H.-M.; Ren, W. Large-Area High-Quality 2D Ultrathin Mo₂C Superconducting Crystals. *Nat. Mater.* **2015**, *14*, 1135–1141.
- (7) Wang, T.; Wang, J.; Chen, W.; Zheng, X.; Wang, E. A Reusable N-Doped-Carbon-Coated Mo₂C Composite Counter Electrode for High-Efficiency Dye-Sensitized Solar Cells. *Chem. Eur. J.* **2017**, 23, 17311–17317.
- (8) Lee, H.-J.; Shim, H.-W.; Kim, J.-C.; Kim, D.-W. Mo-MoO₃-Graphene Nanocomposites as Anode Materials for Lithium-Ion Batteries: Scalable, Facile Preparation and Characterization. *Electrochim. Acta* **2017**, *251*, 81–90.
- (9) Kwak, W.-J.; Lau, K. C.; Shin, C.-D.; Amine, K.; Curtiss, L. A.; Sun, Y.-K. A Mo₂C/Carbon Nanotube Composite Cathode for Lithium—Oxygen Batteries with High Energy Efficiency and Long Cycle Life. *ACS Nano* **2015**, *9*, 4129–4137.
- (10) Tuomi, S.; Guil-Lopez, R.; Kallio, T. Molybdenum Carbide Nanoparticles as a Catalyst for the Hydrogen Evolution Reaction and the Effect of Ph. *J. Catal.* **2016**, 334, 102–109.
- (11) Schaidle, J. A.; Blackburn, J.; Farberow, C. A.; Nash, C.; Steirer, K. X.; Clark, J.; Robichaud, D. J.; Ruddy, D. A. Experimental and Computational Investigation of Acetic Acid Deoxygenation over Oxophilic Molybdenum Carbide: Surface Chemistry and Active Site Identity. ACS Catal. 2016, 6, 1181–1197.
- (12) Murugappan, K.; Mukarakate, C.; Budhi, S.; Shetty, M.; Nimlos, M. R.; Román-Leshkov, Y. Supported Molybdenum Oxides as Effective Catalysts for the Catalytic Fast Pyrolysis of Lignocellulosic Biomass. *Green Chem.* **2016**, *18*, 5548–5557.
- (13) Shetty, M.; Murugappan, K.; Prasomsri, T.; Green, W. H.; Román-Leshkov, Y. Reactivity and Stability Investigation of Supported Molybdenum Oxide Catalysts for the Hydrodeoxygenation (HDO) of m-Cresol. *J. Catal.* **2015**, 331, 86–97.
- (14) Prasomsri, T.; Shetty, M.; Murugappan, K.; Román-Leshkov, Y. Insights into the Catalytic Activity and Surface Modification of MoO₃ during the Hydrodeoxygenation of Lignin-Derived Model Compounds into Aromatic Hydrocarbons under Low Hydrogen Pressures. *Energy Environ. Sci.* **2014**, *7*, 2660–2669.
- (15) Gao, J.; Zheng, Y.; Fitzgerald, G. B.; de Joannis, J.; Tang, Y.; Wachs, I. E.; Podkolzin, S. G. Structure of Mo_2C_x and Mo_4C_x Molybdenum Carbide Nanoparticles and Their Anchoring Sites on ZSM-5 Zeolites. *J. Phys. Chem. C* **2014**, *118*, 4670–4679.
- (16) Lunsford, J. H. Catalytic Conversion of Methane to More Useful Chemicals and Fuels: A Challenge for the 21st Century. *Catal. Today* **2000**, *63*, 165–174.
- (17) Spivey, J. J.; Hutchings, G. Catalytic Aromatization of Methane. *Chem. Soc. Rev.* **2014**, 43, 792–803.
- (18) Ismagilov, Z. R.; Matus, E. V.; Tsikoza, L. T. Direct Conversion of Methane on Mo/ZSM-5 Catalysts to Produce Benzene and Hydrogen: Achievements and Perspectives. *Energy Environ. Sci.* **2008**, 1, 526–541.
- (19) Weckhuysen, B. M.; Wang, D.; Rosynek, M. P.; Lunsford, J. H. Conversion of Methane to Benzene over Transition Metal Ion ZSM-5 Zeolites: II. Catalyst Characterization by X-Ray Photoelectron Spectroscopy. *J. Catal.* **1998**, *175*, 347–351.

- (20) Weckhuysen, B. M.; Wang, D.; Rosynek, M. P.; Lunsford, J. H. Conversion of Methane to Benzene over Transition Metal Ion ZSM-5 Zeolites: I. Catalytic Characterization. *J. Catal.* **1998**, *175*, 338–346.
- (21) Tempelman, C. H. L.; Hensen, E. J. M. On the Deactivation of Mo/HZSM-5 in the Methane Dehydroaromatization Reaction. *Appl. Catal., B* **2015**, *176-177*, 731–739.
- (22) Lezcano-González, I.; Oord, R.; Rovezzi, M.; Glatzel, P.; Botchway, S. W.; Weckhuysen, B. M.; Beale, A. M. Molybdenum Speciation and Its Impact on Catalytic Activity During Methane Dehydroaromatization in Zeolite ZSM-5 as Revealed by Operando X-Ray Methods. *Angew. Chem., Int. Ed.* **2016**, *55*, 5215–5219.
- (23) Kosinov, N.; Coumans, F. J. A. G.; Li, G.; Uslamin, E.; Mezari, B.; Wijpkema, A. S. G.; Pidko, E. A.; Hensen, E. J. M. Stable Mo/HZSM-5 Methane Dehydroaromatization Catalysts Optimized for High-Temperature Calcination-Regeneration. *J. Catal.* **2017**, 346, 125–133.
- (24) Gao, J.; Zheng, Y.; Tang, Y.; Jehng, J.-M.; Grybos, R.; Handzlik, J.; Wachs, I. E.; Podkolzin, S. G. Spectroscopic and Computational Study of Cr Oxide Structures and Their Anchoring Sites on ZSM-5 Zeolites. *ACS Catal.* **2015**, *5*, 3078–3092.
- (25) Lacheen, H. S.; Iglesia, E. Isothermal Activation of ${\rm Mo_2O_5}^{2+}$ ZSM-5 Precursors During Methane Reactions: Effects of Reaction Products on Structural Evolution and Catalytic Properties. *Phys. Chem. Chem. Phys.* **2005**, *7*, 538–547.
- (26) Ma, D.; Shu, Y.; Cheng, M.; Xu, Y.; Bao, X. On the Induction Period of Methane Aromatization over Mo-Based Catalysts. *J. Catal.* **2000**, *194*, 105–114.
- (27) Kosinov, N.; Coumans, F. J. A. G.; Uslamin, E. A.; Wijpkema, A. S. G.; Mezari, B.; Hensen, E. J. M. Methane Dehydroaromatization by Mo/HZSM-5: Mono- or Bifunctional Catalysis? *ACS Catal.* **2016**, 7, 520–529.
- (28) Ding, W.; Meitzner, G. D.; Iglesia, E. The Effects of Silanation of External Acid Sites on the Structure and Catalytic Behavior of Mo/H–ZSM5. *J. Catal.* **2002**, 206, 14–22.
- (29) Ding, W.; Li, S.; D Meitzner, G.; Iglesia, E. Methane Conversion to Aromatics on Mo/H-ZSM5: Structure of Molybdenum Species in Working Catalysts. *J. Phys. Chem. B* **2001**, *105*, 506–513. (30) Tan, P. L.; Wong, K. W.; Au, C. T.; Lai, S. Y. Effects of Co-Fed O₂ and CO₂ on the Deactivation of Mo/HZSM-5 for Methane Aromatization. *Appl. Catal.*, *A* **2003**, 253, 305–316.
- (31) Lacheen, H. S.; Iglesia, E. Stability, Structure, and Oxidation State of Mo/H-ZSM-5 Catalysts during Reactions of CH₄ and CH₄–CO₂ Mixtures. *J. Catal.* **2005**, 230, 173–185.
- (32) Liu, Z.; Li, L.; Iglesia, E. Catalytic Pyrolysis of Methane on Mo/H-ZSM5 with Continuous Hydrogen Removal by Permeation through Dense Oxide Films. *Catal. Lett.* **2002**, *82*, 175–180.